Optimal control for optical structures

6.1   In search of the optimal structuring tool

In Ch. 4 the effects of various irradiation conditions were explored (energy per pulse, number of shots per site, repetition rate, pulse duration and focusing depth). In Ch. 5 we investigated the intrinsic material response. The importance of thermomechanical phenomena was highlighted. In this way, a guideline for the timescales of energy relaxation was obtained. We now exploit the possibility to control the succession of thermodynamic and thermomechanical transformations by performing a temporal design of the excitation sequence. The final purpose is to achieve control on laser-induced refractive index changes while synchronizing energy income and material response. As a main difficulty, the complexity involved during laser-matter interaction (in particular the nonlinear propagation and response of the material) prevents from establishing a direct relation between an initial excitation sequence and the final laser-induced phase object. Therefore, a theoretical design of laser sequence is not realistic at this point.

To bypass this difficulty we use a concept first reported by Judson and Rabitz [102] in the frame of femtochemistry studies, for molecular control. As optimal control of molecules can not be achieved from theoretical design, due to the extreme complexity of molecular Hamiltonians for multi atomic systems, Judson and Rabitz proposed to perform an experimental search and try procedure. An apparatus able to evaluate the result of the shaped pulse on the experiment reports it to a self-learning algorithm. In return, the algorithm alters the temporal aspect of the electric field. Iterations are performed until the proper experimental
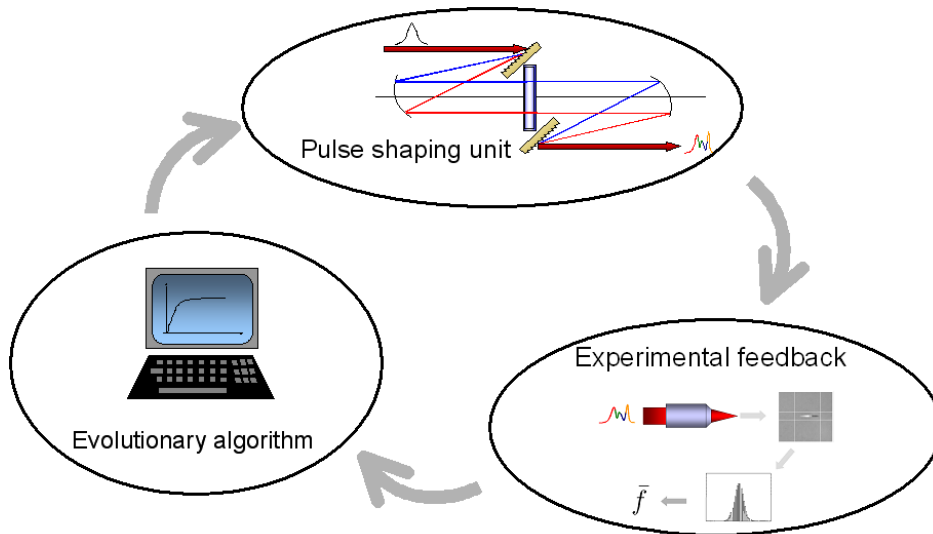
Figure 6.1: Adaptive closed-loop setup including a pulse shaping apparatus.

output is reached (see Fig. 6.1).

This chapter presents the concepts of adaptive optimization in the temporal domain and the experimental implementation. It additionally describes experimental results from the viewpoint of the design of refractive index change with controlled axial characteristics.

6.1.1   Short introduction to evolutionary algorithms

A delicate aspect is the choice of a suitable optimization strategy because of the few informations available a priori on the properties of the search space (topology, continuity...). To this extent, evolutionary algorithms exhibit excellent advantages and notably an outstanding robustness.

Evolutionary algorithms are inspired from the principles of biological evolution. As a golden rule, only individuals well adapted to the constraints of their environment survive [103]. The appropriated terminology borrows its nomenclature from the Darwinian evolution theory. In a few words, evolutionary algorithms successively test an ensemble of solutions (a population of individuals) at each iteration (generation). At the end of one generation, the fittest individuals are used as a basis for constituting a new population. The constitution of a new generation is partially probabilistic, rendering the search path used by the program unpredictable and not reproducible. Among the different implementations of this basic idea [104], we used evolution strategies (ES).

The learning algorithm described in this section was implemented with LabView. The main part of the Evolutionary Strategies presented here has been developed at the Freie
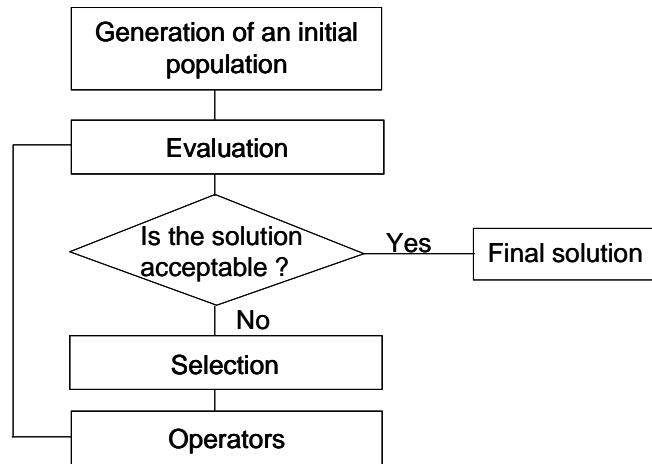
Figure 6.2: Evolutionary algorithm flowchart.

Universität Berlin, and was already used for other purposes [105, 106]. Our contribution is the adaption of the learning algorithm to the environmental setup. This implies the encoding and evaluation steps detailed in Sec. 6.2.3 as well as a relevant choice of initial optimization parameters (See Sec. 6.3).

6.1.2 Building blocks of evolution strategies

Overview

The building blocks presented in Fig. 6.2 are common to all types of evolutionary algorithms (genetic algorithms, evolutionary programming, evolution strategies, genetic programming). The differences lie in the implementation of those basic components. In this section, the emphasis is put on the ES algorithm used for our experiments.

Initial population

The very first population is generally constituted of random individuals. A priori knowledge of the problem to solve can be used in this step in order to generate an initial population with an increased fitness. Another possibility is to include some previous optimization results (called a "recycled individual") in the starting population to check, for instance, whether this solution corresponds to a global maximum. In the frame of our experiments, we frequently introduce a Fourier-limited pulse in the initial population, because it corresponds the standard situation from which improvements are expected.

Representation of an individual

When performing optimization with ES, each individual is represented by a one dimensional real-valued vector organized in three sub arrays: chromosome, variability, and fitness. The first sub array ($\bar{x}$) contains the representation of a solution coded over n values called genes. Following a biology-oriented terminology, a gene corresponds to a location on the chromosome (locus) and the value of a given gene is an allele. The encoding procedure resulting in $\bar{x}$ will be detailed at a later point. The second sub array carries n strategy parameters ($\bar{\sigma}$) used by the mutation operator. Finally, the fitness value $\bar{f}$ of the individual is represented by a scalar. Hence, the structure of one individual can be summarized under the form (adapted from [104])

$$\langle \underbrace{x_1, ..., x_n}_{\bar{x}}, \underbrace{\sigma_1, ..., \sigma_n}_{\bar{\sigma}}, \underbrace{f}_{\bar{f}} \rangle. \tag{6.1}$$

Evaluation

Evaluation corresponds to the conversion of an experimental response into a fitness number. It consists in a rating procedure assigning every individual a level of performance based on an experimental feedback. The output of the evaluation step is the basis to determine whether a solution is adapted, and serves as a primary element to perform selection.

Selection

Once every individual is properly rated, the selection process is in charge to select a group of individuals (called a mating pool) as a basis for generating the next population. By analogy with biology, the selection step is the process where p parents are selected to generate offspring. Beyond the parent selection mechanism, selection also involves the designation of survivors, i.e. individuals directly transmitted to the next generation. The number of survivors s is a free parameter. We usually keep intact one individual to ensure that the best solution of a generation g is at least as good as the best solution from generation $(g-1)$. The selection rules we use are purely elitist, meaning that only the fitness level enters into consideration. The individuals constituting a population are simply ranked according to their fitness and the s best solutions are selected as survivors whereas the p best solutions are exploited to engender new individuals.

Termination condition

The search is stopped in two cases, if the fitness of one individual is higher or equal to an arbitrary value or if the diversity of the population becomes to low. The diversity of the
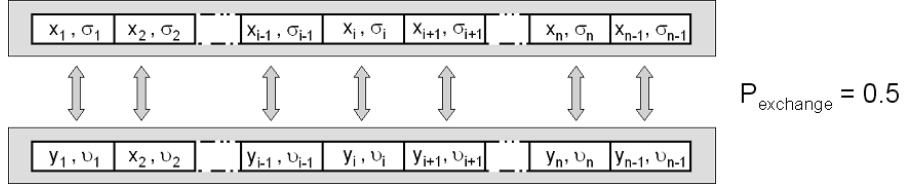
Figure 6.3: Illustration of discrete crossover between two parents. The random allele exchange results in the creation of two new offspring.

population is estimated by comparing the lowest fitness value ($\bar{f}_{min}$), the highest fitness value ($\bar{f}_{max}$) and the average fitness ($\bar{f}_{mean}$) of the current generation. The search is interrupted when those three indicators are significantly close to each other, e.g. within 5 to 10 % .

Variation operators: crossover and mutations

Variation operators are the tools to generate new individuals, i.e. for testing new points of the search space. In contrast to the initial population, a new population is created by mixing (crossover) and modifying (mutations) parts of pre-existing solutions [107]. Variation operators are not applied to survivors.

The crossover is a blend between two parents picked up randomly among the members of the mating pool. Every couple of parents produces two offspring by transmitting randomly each of its pairs (x_i, σ_i) to one or the other offspring with an equal probability (see Fig. 6.3). In this way, the length of a transmitted chain of chromosomes is also random. This method is called discrete crossover. While crossover introduces new combinations of alleles, mutations introduces new alleles based on older alleles. In our case, mutations take place in two steps involving two distinct functions. One function simply consists in multiplying one single random allele x_i by a user-determined mutation factor m_f such as $0.5 < m_f < 1$, mimicking an error in the transmission of the chromosome.

The second function is based on a noise generator $N(\sigma)$ (see Fig. 6.4). Every allele x_i is replaced by

$$x_i' = x_i + N(\sigma_i) = x_i + \sigma_i \times \Gamma(r, y). \tag{6.2}$$

The scalar $\Gamma(r, y)$ is a random number drawn from a distribution with a probability density function $p(\Gamma)$ defined by

$$p(\Gamma) = y\sqrt{\frac{-2\log(r)}{r}}, r \in]0; 1[\tag{6.3}$$

where y is a random number drawn with a uniform probability in the interval $[-1; 1]$. The role of σ_i is to set the width of the $p(\Gamma)$ distribution and hence to influence the global mutation amplitude, playing a crucial role in the exploration of the search space.
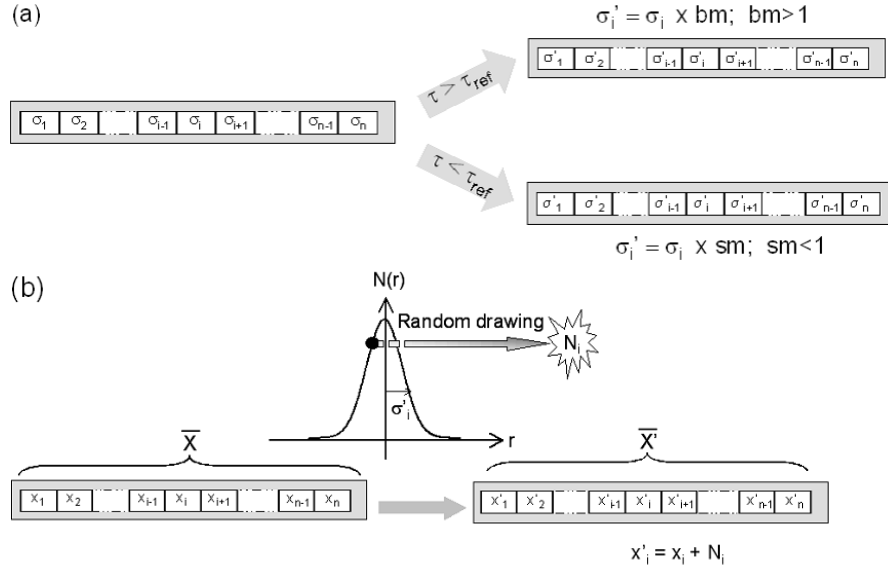
Figure 6.4: Scheme of the mutation operator. The strategy parameters $\bar{\sigma}$ are mutated first (a) and serve as a basis for mutating $\bar{x}$ (b).

At a generation g, $\sigma_i(g)$ writes

$$\sigma_i(g) = \begin{cases} \sigma_0 & \text{if } g = 0, \\ \sigma_i(g-1) & \text{if the individual is a survivor,} \\ \sigma_i(g-1) \times \alpha_g & \text{otherwise.} \end{cases} \qquad (6.4)$$

The coefficient σ_0 is fixed by the user before the optimization starts. The value of α_g drives the whole mutation process and can take the two user-determined values sm (small mutation) and bm (big mutation). Whether sm or bm applies for one generation depends on the learning rate τ and

$$\alpha_g = \begin{cases} sm & \text{if } \tau < \tau_{ref}, \\ bm & \text{otherwise.} \end{cases} \qquad (6.5)$$

The evaluation of the learning rate τ simply corresponds to the fraction of the population with a higher fitness than the previous generation and τ_{ref} is set to the convenience of the user to a value corresponding to an average expected learning rate.

We emphasize that the set of strategy parameters $\bar{\sigma}$ is adaptive i.e. coevolves with the search process. Typically, as the population converges toward an optimum, the learning rate is slower than at the beginning of the optimization, when improving the search results is facile. As a consequence, τ tends to decrease with g, translating into smaller steps in the search space via smaller values of α_g.

6.2 Implementation of the adaptive pulse shaping strategy

In this section, the emphasis is put on the links bridging the algorithm to the real world, namely the encoding and the experimental feedback.

6.2.1 Encoding excitation sequences into virtual individuals

Alphabet used by the algorithm

The step of encoding simply consists in translating a temporal envelope into a one dimensional real-valued vector of size n, corresponding to the sub array $\bar{x}$ in the expression 6.1. In Sec. 3.1.2, we highlighted the role of the spatial light modulator (SLM) for performing pulse shaping. This device includes a serial port which offers the possibility to set arbitrary phase masks from a PC by individually assigning a value to each of the 640 pixels constituting the SLM. Originally, each pixel can be driven in one state among 2^{12}.

The algorithm works with real values x_i such as $0 \leq x_i \leq 1$ before transforming them into 12 bits integers. At first, a simple multiplication by 2π turns each x_i into a phase value and in a second step, the final transformation from phase values into drive values is ensured via the calibration curve of the SLM. A discretization takes place, with a maximum quantization error Q of

$$Q = \frac{S_{max}}{2N_d}, \tag{6.6}$$

where N_d is the number of drive values and S_{max} is the highest value of the signal to quantify. In the x_i space, $S_{max} = 1$ and in the phase space, $S_{max} = 2\pi$. The value of Q will be used at a later point, when setting the parameter sm presented in Sec. 6.1.2.

Size of the search space

The dephasing induced by one pixel being coded on 12 bits, i.e. over $N_d = 2^{12}$ discrete values, the size of the search space ($\mathcal{S}$) is initially of

$$\mathcal{S} = N_d^{n_{pix}} = (2^{12})^{640} = 4096^{640}, \tag{6.7}$$

n_{pix} corresponding to the number of active pixels on the SLM.

The first task to perform is obviously to attempt reducing $\mathcal{S}$. The example developed in this section corresponds to the experimental conditions when working with System I, but the same strategy was applied when implementing the ES onto system IV.

Firstly, the maximal phase delay is restricted from 6π to 2π within the steepest part of the SLM calibration curve, efficiently shrinking down N_d to 300. As a drawback, lowering N_d results in an increase of Q (see Eq. 6.6).

Furthermore, additional improvements are possible exploiting the fact that only a fraction of the SLM (250 pixels out of 640) is effective, because of the narrow laser bandwidth. This allows to decrease $\mathcal{S}$ down to 300^{250} points.

The last process reduces the length of a representative string by grouping pixels. The principle is to create superpixels by binning k adjacent pixels, at the expense of the spectral resolution. This also limits the class of reachable solutions notably because of the Nyquist criterion, forbidding phase jumps higher than π between two adjacent pixels [108]. Practically, an important refinement is implemented into the grouping operator to partially compensate this restriction. Instead of equalizing k adjacent pixels, a linear interpolation is performed between the two boundaries of the superpixel. Although this does not bring any benefit regarding $\mathcal{S}$, linear interpolation ensures the respect of the Nyquist criterion for $k > 2$ as the maximal jump between two adjacent pixels is then of $\Delta\varphi = \frac{2\pi}{k}$.

Conclusion: representation of the chromosome $\bar{x}$

Finally, $\bar{x}$ vectors are real-valued strings of $\frac{250}{k}$ elements. Because of the discrete nature of the phase pattern, each element can take 300 distinct values, leading to a final search space size $\mathcal{S}$ of

$$\mathcal{S} = 300^{\frac{250}{k}}. \tag{6.8}$$

6.2.2   Definition of a valuable solution

Translation of the experimental feedback

The last element missing to the adaptive setup is the translation of the laser action into a relevant selection criterion for the algorithm. The post-irradiation diagnosis is carried out by a system including a phase-contrast microscope (see Sec. 3.3.2). Phase-contrast microscopy (PCM) translates the refractive index map of the laser-imprinted object into grey values. Therefore, the evaluation procedure is simply in charge of converting the PCM information into a scalar value $\bar{f}$ (introduced in the expression 6.1) for each individual.

Pixel-based fitness evaluation

This type of evaluation strategy relies on the analysis of a region of interest (ROI) limited to the vicinity of the laser-induced trace. Within this region, the number of white pixels (n_w)
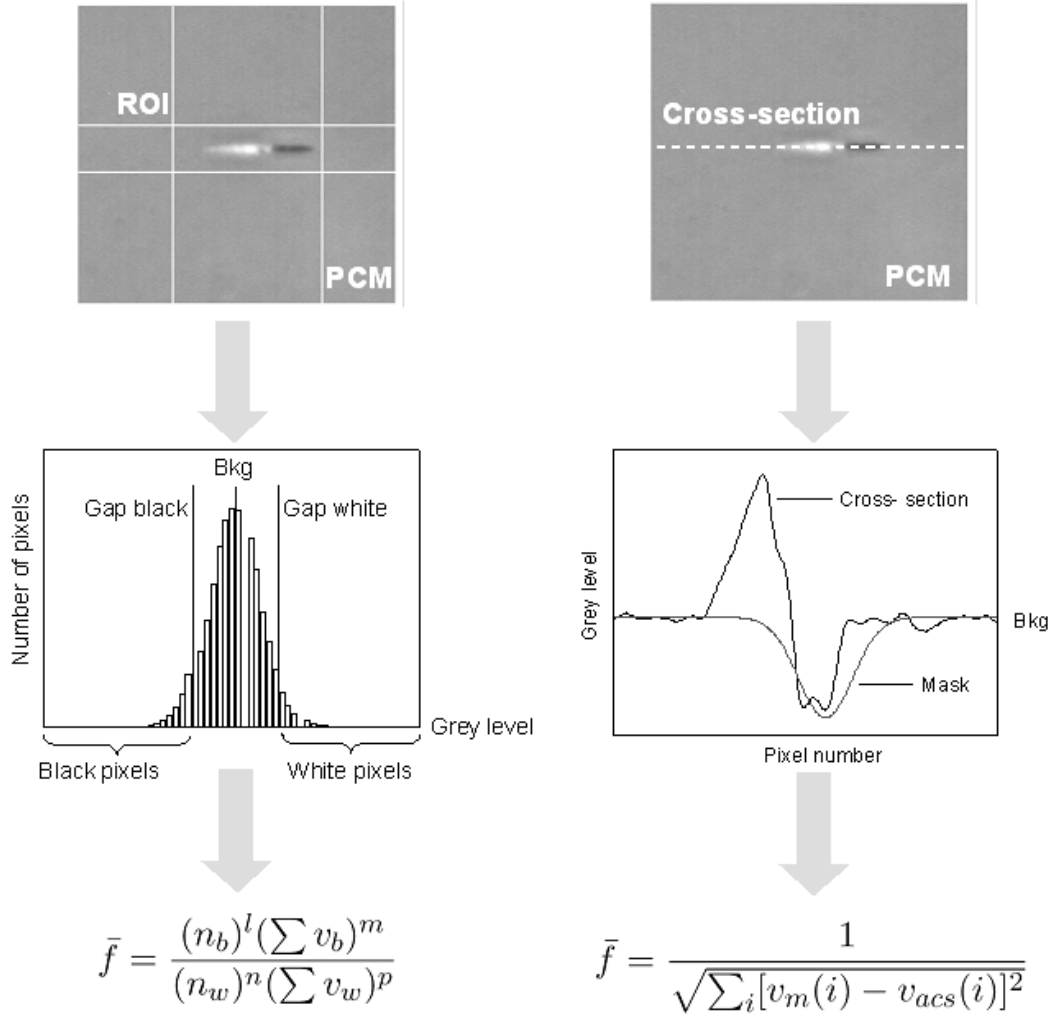
Figure 6.5: Procedure of fitness assignments based on pixel evaluation (left) and on target mask resemblance (right).

and the number of black pixel (n_b) serve as a basis for the calculation of the fitness value $\bar{f}$ according to

$$\bar{f} = \frac{(n_b)^l (\sum v_b)^m}{(n_w)^n (\sum v_w)^p} \quad , \qquad l, m, n, p \in \mathbb{R}. \tag{6.9}$$

Values of l, m, n and p are free parameters arbitrarily set by the user. The terms $\sum v_b$ and $\sum v_w$ correspond to the sum of the grey levels of the black and the white pixels, respectively. In despite of an apparent complexity, Eq. 6.9 proves to be a very flexible fitness function, allowing varied fitness evaluations from a single function. The class (white or black) of a pixel is determined by thresholding around the mean background value bkg (see Fig. 6.5). If the grey value of a pixel is below (above) the value of the background augmented by a safety gap, the pixel is considered as black (white).

Mask-based fitness evaluation

This method is oriented toward a global design of the final optical structure. The on-axis refractive index profile imprinted by a potential solution (called axial cross-section in this section) is compared to a user-designed target (mask). The fitness value $\bar{f}$ depends on the distance between the axial cross-section and the mask defined by (see Fig. 6.5)

$$\bar{f} = \frac{1}{\sqrt{\sum_i [v_m(i) - v_{acs}(i)]^2}},$$
(6.10)

where $v_m(i)$ and $v_{acs}(i)$ are respectively the grey values of the mask and of the axial cross-section at the pixel i in the grey-level image. One difficulty is the choice of an origin for the i axis. Details on the relative positioning of the mask and of the axial cross-section will be given at a later point.

6.2.3   Experimental constraints on the maximum optimization time

The major restrictions encountered when setting up this experiment have mainly two distinct origins which are the space available on the sample and the total optimization time.

Restrictions due to the geometry of the sample

The experimental apparatus is described in Sec. 3.4. The sample is initially 20 mm long but because of the sample holder and because working in the immediate vicinity of the edges is disturbing the PCM observation, a maximum length of 17 to 18 mm is effectively available. The adaptive optimizations are carried out in irradiation conditions relevant for technological applications. Therefore, the input energy is typically around 0.5 μJ. As the affected zone is very localized around the propagation axis, a spacing of 5 to 10 μm between two consecutive traces is sufficient to ensure that the focused excitation sequence interacts with a fresh bulk and that the evaluation takes place in adequate conditions. Hence, a minimum of 1700 individuals can be tested in a single column. This may possibly be insufficient to satisfy one of the termination conditions presented in Sec. 6.1.2. Therefore, the optimization can be out on several columns. Because of spherical aberrations, the last column should not be located deeper than 0.2 mm in the bulk. Moreover, the first column should be far enough from the entrance of the sample so that the surface does not drastically influence the laser-matter interaction mechanisms. Depending on the average length of the laser-imprinted trace, up to 3 columns separated by 30 μm can be used for low input energies (0.3 to 0.5 μJ). When higher energies are used, the optimization can be carried out over 2 columns only.

As a summary, the maximum number of individuals n_{max} that can be tested in a single sample layer is of 3400$< n_{max} <$10200.

Total optimization time

Testing an individual implies setting the proper phase pattern on the SLM, move and stabilize the sample, irradiate and evaluate the fitness. With a proper task synchronization, a 1 Hz testing rate is attained. It means that an optimization run takes about 1 to 4 hours. During this time, it is fundamental to guarantee a stable environment. The laser-beam characteristics, the lightening of the microscope, the imaging and writing planes and finally the positioning and movement of the sample have to be kept perfectly constant.

6.3   Configuration of the algorithm

Although the choice of a proper set of optimization parameters obviously depends on the task to achieve, the experimental environment helps in setting a basic parameter set. Fine adjustments required to satisfy a particular case will be specified when needed.

Population size

The size of the population Ω is equal to the sum of the number of survivors μ with the number of offspring λ. It corresponds to the number of solutions tested at each iteration. In general, a high value of Ω implies a good degree of diversity between the individuals and therefore the risks to converge on a local optimum are minimized. This is an indisputable advantage when the search space exhibits a multimodal topology. As a drawback, the space used on the sample at each iteration is increased, limiting the maximum number of iterations. A satisfying point of equilibrium is found around $\lambda = 30$ and $\mu = 1$. The number of survivors is limited to one in order to avoid a cannibalization effect, i.e. that the alleles of a small group of fit individuals gets rapidly over-represented in the population. The size of the initial population Ω_0 does not influence Ω, but Ω_0 should be high enough to warrant the diversity within the first mating pool. A minimum value of $\Omega_0 = \lambda/2$ is normally set. Our initial population is composed of random individuals but also of one "recycled individual" which corresponds to a phase pattern producing a Fourier-limited pulse.

Mutation parameters

Mutation parameters are extremely delicate to set and usually decisive in the search success. The parameter m_f is restricted to the interval $0.5 < m_f < 1$ and seem to play a role which is more conceptual than practical. Although we could not see a drastic influence of this parameter on the global convergence of the algorithm, we usually set $m_f = 0.9$. The two parameters sm and bm defined in Sec. 6.1.2 set the exploration stepsize. The adaptive

mechanism ruling the mutations amplitude only make sense when $sm < 1 < bm$. Again, there is a tradeoff between fast convergence and risk to converge on a local optimum. To this extent, the values $0.7 < sm < 0.8$ and $1.2 < bm < 1.3$ seem to be reasonable. The expected learning rate τ_{ref} is generally set to about $\tau_{ref} = 0.3$. This value usually ensures a well balanced role between bm and sm. The initial value of the mutation step σ_0 determines around which amplitude the mutations evolve. If σ_0 is too small then mutations are not significant and their effect is lost during the discretization process (see Sec. 6.2.1) while a value of σ_0 too high leads to a saturation phenomenon and all the x_i are rapidly binary taking either the value $x_i = 0$ or $x_i = 1$. A good compromise is reached for $\sigma_0 = 0.003$.

The standard set of parameters is summarized in Tab. 6.1.

Table 6.1: Standard parameters of the evolutionary strategies used for performing adaptive pulse shaping experiments.

	Parameter	Value
	Number of recycled individuals	1
Population Size	Size of the initial population (Ω_0)	15
	Number of offspring (λ)	30
	Number of survivors (s)	1
	Initial strategy parameter (σ_0)	0.003
	Reference learning rate (τ_{ref})	0.3
Mutation parameters	Small mutation step (sm)	0.7-0.8
	Big mutation step (bm)	1.2-1.3
	Multiplication factor (m_f)	0.9

6.4   Optimization results in a-SiO$_2$

6.4.1   High refractive index structures in a weak aberrations regime

In a general way, positive refractive index structures are relevant for technological applications using direct laser-writing of optical components (see for instance [109] and references therein). Some tunability in the amplitude of the refractive index modulation Δn would be very interesting. Therefore, we now search for irradiation conditions leading to a positive Δn of maximal amplitude, as a first step toward a toolbox of temporal shapes inducing arbitrary refractive index modulations when focused in the bulk of fused silica.

Optimization criterion and experimental conditions

System I was used to perform this series of optimizations. We performed several optimizations using fitness functions based on pixel evaluation. Invariably, the Fourier-limited pulse (SP) is the most adequate temporal shape. Blind optimizations (i.e. with no SP included in the initial population) did not produce solutions as good as a SP. Therefore, we tried to perform optimizations using a mask-based fitness function (see Sec. 6.2.2). The target, i.e. the on-axis refractive index profile we try to reach, has a Gaussian profile. For comparing the trace with the mask, the lowest minima of the axial grey-level cross-section is aligned with the lowest point of the Gaussian mask. Aberrations were minimized by focusing at a depth of 170 μm in the bulk. The laser pulse energy is limited to 0.4 μJ, close to the detectable modification threshold. A SP is introduced in the initial population.

Results and discussion

After 50 iterations, the fitness of the best individual is multiplied by 1.5 with respect to the fitness of the SP. As shown from the results presented in Fig. 6.6, the amplitude of Δn could not be significantly improved, confirming the few success obtained with simple pixel-based evaluation functions. Nevertheless, there exists a good flexibility regarding the length of the dark filament. This is potentially interesting when writing waveguides in a transversal configuration, as the ellipticity of the guide is detrimental for the symmetry of the propagating modes [68]. Although the OP temporal profile looks quite similar to a broadened single pulse, the same type of structures could not be reproduced only by varying the pulse duration or the laser pulse energy. This emphasizes the role of nonlinear propagation and plasma generation. Therefore, as we mentioned earlier in this chapter, it is difficult to establish a direct connection between temporal excitation and effective energy deposition. Such a correlation would necessitate using the propagation code presented in Sec. 2.4.1 with the optimal temporal shape (see Fig. 6.6) as an input.

6.4.2   High refractive index structures in a-SiO$_2$ in presence of aberrations

Although a group of authors [65] proposed to exploit the effects of spherical aberrations, they are usually a limiting factor, especially for two reasons. Firstly, the axial dimension of the trace results in strongly elliptical guiding structures in transverse writing configuration and secondly, the density of energy in the focal volume being smaller, the subsequent amplitude of refractive index modulation Δn is reduced. We suggest, as a first step, to maximize the
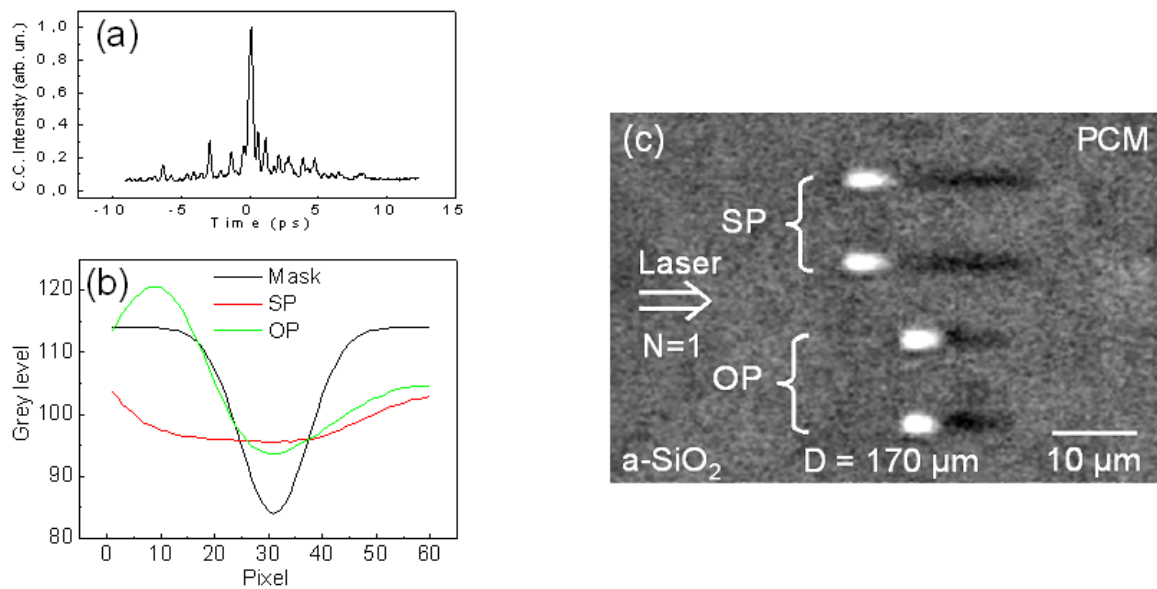
Figure 6.6: (a): Temporal intensity distribution produced by the optimal solution in a single irradiation sequence. (b): Comparison of the axial cross-sections induced by a short pulse (SP) with a FWHM duration of 200 fs and the optimal pulse (OP) with the target (b). (c): Phase contrast microscopy (PCM) observation of traces induced by a short pulse (SP) and an optimal pulse (OP) with a laser pulse energy of 0.4 μJ. Aberrations are minimized by focusing at D=170 μm in the bulk.
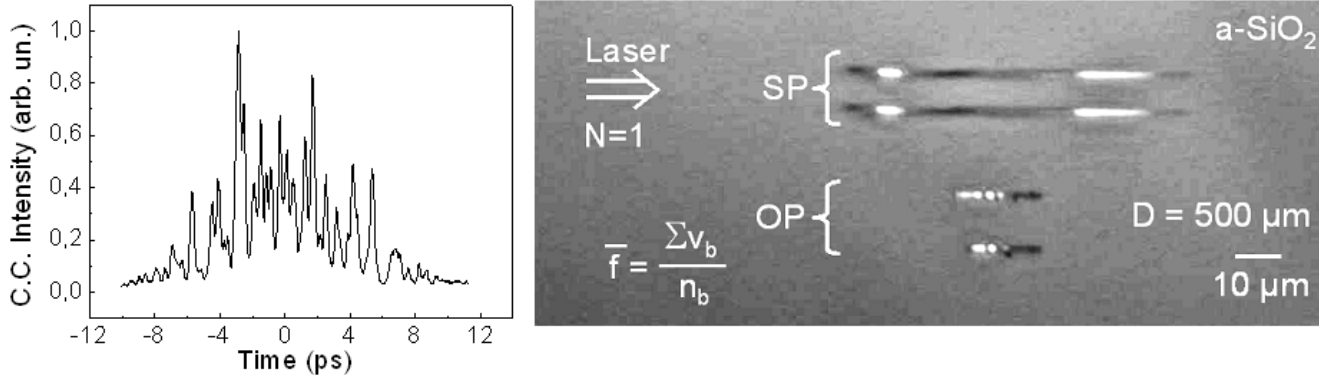
Figure 6.7: Temporal intensity distribution produced by the optimal solution in a single irradiation sequence (left). The laser pulse energy is limited to 1.4 μJ. On the right, PCM observation of traces induced by a short pulse (SP) with a FWHM duration of 200 fs and an optimal pulse (OP). Aberrations are enhanced by focusing at D=500 μm in the bulk.

amplitude of the refractive index modification in presence of aberrations.

Optimization criterion and experimental conditions

We use a fitness function based on pixel evaluation. The objective is to maximize the average of Δn in the irradiated zone, for positive Δn only. We translate this goal by setting $l = -1$, $m = 1$, $n = 0$, $p = 0$ in Eq. 6.9. In this fashion, $\bar{f}$ directly corresponds to the average value of the black pixels. At first, the region of interest (ROI), i.e. the region in which pixels are counted (see Sec. 6.2.2), is a rectangle of about 10×80 μm^2 centered around the propagation axis. It appears that this choice of ROI greatly favored solutions resulting in shock affected regions as they exhibit a very dark appearance in PCM (see for instance Fig. 4.4). Therefore, the individuals corresponding to long duration pulses were well ranked by the algorithm, despite of an important number of white pixels. To overcome this problem, the ROI was restricted to a long but narrow rectangle centered with respect to the propagation axis. The laser pulse energy is limited to 1.4 μJ and the aberrations are maximized by focusing 0.5 mm into the bulk material.

Results, observations and complementary investigations

The optimal temporal shape as well as the resulting traces visible in PCM are shown in Fig. 6.7. Those results imply the following. Firstly, we underline that the initial goal, i.e. to increase the average Δn in the modified region has been successfully reached, although this is at the expense of the size of the imprinted structure. Secondly, while the energy deposition is spread over a time-window of several picoseconds, the final response of the material is
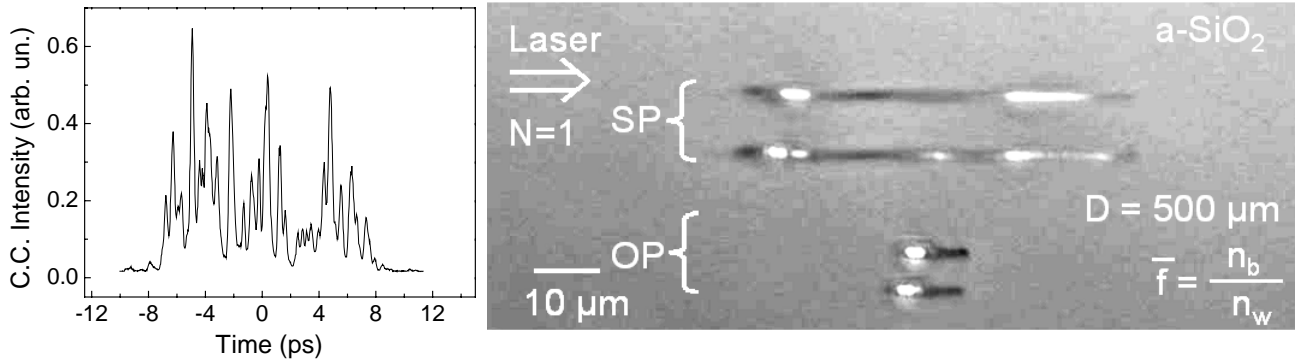
Figure 6.8: Temporal intensity distribution produced by the optimal solution in a single irradiation sequence (left). The laser pulse energy is limited to 1.4 μJ. On the right, PCM observation of traces induced by a short pulse (SP) with a FWHM duration of 200 fs and an optimal pulse (OP). Aberrations are enhanced by focusing at D=500 μm in the bulk.

very different compared to what would be expected in a picosecond irradiation case, as a confirmation of the strong distortions experienced by the OP under nonlinear propagation.

Finally, the PCM observation of the irradiated region shows a noteworthy feature. Even though the energy deposition map in the vicinity of the focal plane is not easily accessible, simple qualitative observations bring interesting clues for understanding the mechanisms of refractive index augmentation. The PCM analysis shows that a series of voids (respectively 4 on the upper trace and 3 on the lower one) appears upon irradiation with the OP. Furthermore, while monitoring online the optimization process, we could not detect any black filament alone, i.e. with no white cavity associated. This questions the interdependence between positive refractive index change and onset of a low index cavity (void).

Therefore, we tried to penalize individuals resulting in the onset of white pixels by setting $l = 1$, $m = 0$, $n = 1$, $p = 0$. In this way, $\bar{f}$ corresponds to the ratio black pixels over white pixels. All other experimental conditions are strictly similar. Results are shown in Fig. 6.8. With respect to a single pulse, the fitness is higher by a factor 3.5. The cross-correlation profile of the optimal pulse (OP) shows that the OP is constituted of a central peak (FWHM about 650 fs) on a picosecond pedestal (about 7ps FWHM). Interestingly, at least one white structure visible in PCM persists. Approximately 30 optimization runs have been carried out in fused silica without generating a single individual resulting in a black trace only. This naturally suggests that *high refractive index filament and presence of a low index cavity are correlated.*

6.4.3   Discussion

In this section, the optimization results we obtained in a-SiO$_2$ are used as a basis for discussing two different aspects of adaptive pulse shaping.

At first, adaptive pulse shaping is considered as a flexible tool for energy deposition and material structuring, and we emphasize the potential technological interest of the results presented earlier in this chapter.

Secondly, the results provided by the optimization algorithm are used as a basis for understanding the mechanisms of laser-matter interaction. In this purpose, a refinement of the scenario suggested in Sec. 4.1.1 for the formation of the high refractive index filament is proposed.

Potential technological interests

As a main result, the results presented in Sec. 6.4.2 show that temporal pulse shaping allows for controlling the length of the high refractive index filament. This flexibility is particularly interesting in presence of strong aberrations. Although it should be emphasized that we do not perform aberration corrections, i.e. wavefront distortions are surely still taking place, we are able to compensate the effects of aberrations on the energy deposition into the bulk. This opens the door to symmetric waveguide writing (i.e. with a circular transverse profile) in presence of aberrations.

In a more general way, it is assumed that controlling the size of the affected region can be relevant for direct-writing of a number of optical components at an arbitrary depth in the bulk, e.g. diffractive lenses [77], or gratings [110].

Furthermore, as the pulse shaping method allows for online modification of the temporal shape, a dynamic correction of spectral phase seems to stand as a relevant concept, with potential benefits for femtosecond laser writing of three-dimensional integrated optics [68].

In conclusion, as the effect of aberrations is minimized, our results suggest that temporal shaping may be an alternative to the utilization of cylindrical lenses [75] for symmetric waveguide writing.

Formation of the high refractive index filament

Based on the correlation observed in Sec. 6.4.1 and Sec. 6.4.2 between void formation and presence of a black filament, we can tentatively improve the scenario proposed in Sec. 4.1.1 for explaining the origin of the high refractive index filament, labeled as region II in Fig. 4.2, under SP irradiation. We support our discussion with the results given by the model presented in Sec. 2.4.1. The sequential energy deposition in the free carriers during irradiation by a 100
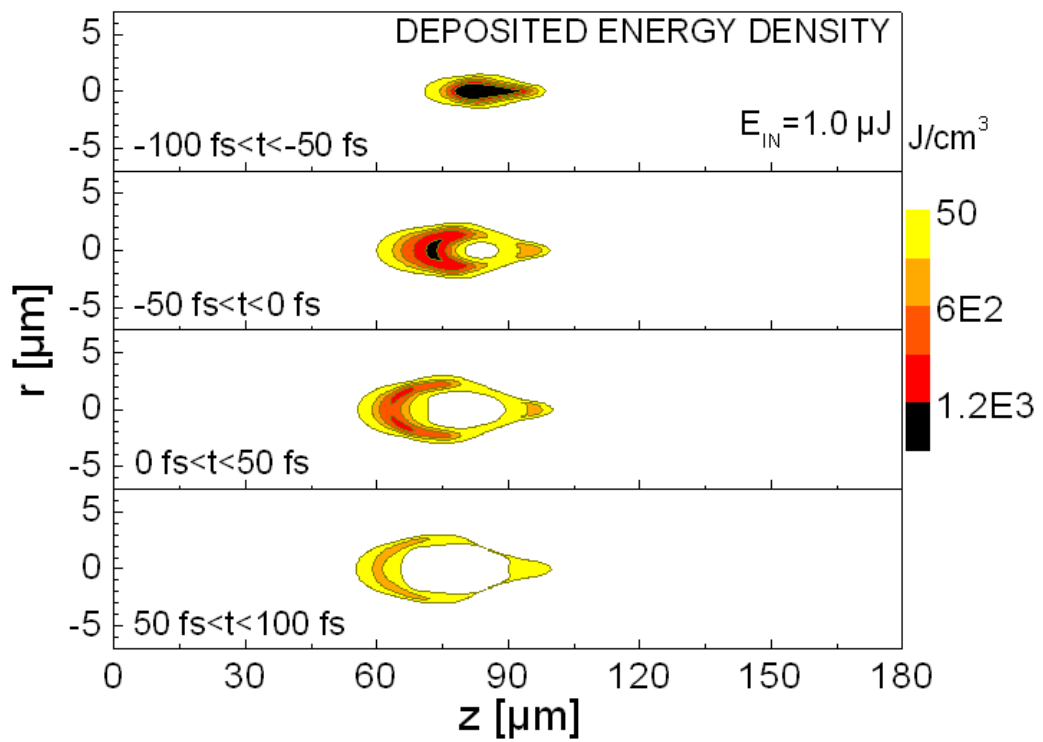
Figure 6.9: Sequential energy deposition in free carriers in irradiated a-SiO$_2$ for a single laser pulse energy of 1 μJ and 120 fs duration. The integration domains are written on the left side of the figure.

fs pulse is shown in Fig. 6.9. At the beginning of the irradiation sequence ($-100 < t < -50$ fs), the intensity is moderated and the energy is mostly deposited around the propagation axis in a channeled region corresponding to the location of the dark filament. Due to the subsequent electronic excitation, the material is softened and exhibits a higher compressibility compared to the pristine bulk. The white cavity associated with the high fluence region in Fig. 4.3 (a) is being gradually induced at later times. When the electrons have transferred their energy to ions, a shock wave emerges from the irradiation zone [82]. When propagating through region II, the interaction of a shock wave with the softened material may result in the onset of point defects [111], vacancy diffusion (Gorsky effect) or in point defects diffusion [112]. This may result in the creation of a high point defect density region. If the density of defects is higher than 1×10^{18} cm^{-3}, a structural relaxation process is triggered, [54], leaving behind a high density material. Hydrodynamic compaction may be triggered as well due to the lack of mechanical resistance on the axial direction.

6.5 Optimization results in BK7

6.5.1 Preliminary experiments in single-shot regime

PCM observations presented in Ch. 4.1.2 emphasize the "thermal" response of BK7 after short pulse (SP) irradiation in standard ultrafast conditions. We remind that a long free carrier decay time was observed for BK7 ($\approx$ 8ps), leading to a soft energy deposition. The irradiated material seems to expand upon the thermoelastic effect and quenches in a low-density, low-refractive index phase upon cooling. Although this is probably due to an intrinsic property of the material (e.g. the high thermal expansion coefficient), we now wish to explore how the energy deposition sequence can influence this natural behavior, particularly detrimental for technological achievements such as waveguide writing. Therefore, the focus is put on inducing a positive refractive index change upon laser irradiation.

Optimization criterion and experimental conditions

In the prospect of achieving waveguide writing in BK7 as a proof of principle, the result of optimizations based on masks are put forward. In this context, the Gaussian profile of the target is particularly relevant, as it follows the refractive index profile of a gradient-index fiber. The input energy is close to the modification threshold visible in PCM, about 350 nJ.
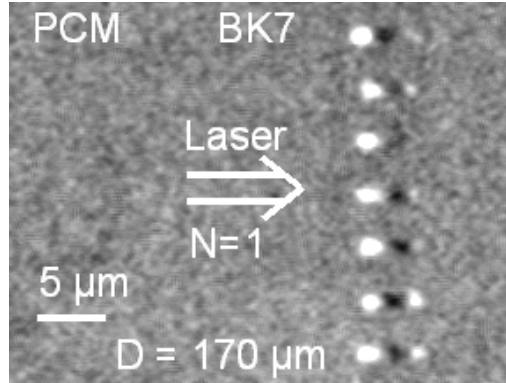
Figure 6.10: PCM observation of the traces imprinted by different individuals after 50 generations in a single shot regime (N=1). The selection criterion is based on a Gaussian mask. The laser pulse energy is limited to 350 nJ. Aberrations are minimized by focusing at D=170 μm in the bulk.

Results

A limited amount of optimizations runs (about 10) were carried out in single-shot regime (with system I) and most of the experimental effort was concentrated on high repetition rate irradiation conditions (presented in the next section), in order to work in the perspective of achieving waveguide writing in viable industrial conditions. In Fig. 6.10, we show the result of a PCM picture taken at the end of an optimization run of about 50 iterations, illustrating that numerous individuals engendered during the evolutionary process fulfill our expectations. Several traces exhibit an on-axis refractive modulated index profile, showing successively negative, positive and negative components. This is obviously an encouraging step toward a low loss guiding structure. In some cases, the refractive index profile is symmetric with a spatial structure showing a convincing degree of similitude with the one of a guiding fiber. We also tried to perform pixel-based optimizations with the number of black pixels as a fitness measurement ($l = 1, m = 0, n = 0, p = 0$ in Eq. 6.9). Surprisingly, the same type of structure (see Fig. 6.12) as in the case of the mask-based fitness evaluation was obtained.

Discussion

According to our previous results, a positive-negative-positive variation of refractive index seems to be an easy target to reach. Unfortunately, ulterior examinations revealed that the second white dot, well visible in Fig. 6.10, can randomly disappear from shot to shot. Furthermore, it was observed that for a given temporal shape, this feature appears in a very narrow processing window only. Even though a complete study was not carried out, we
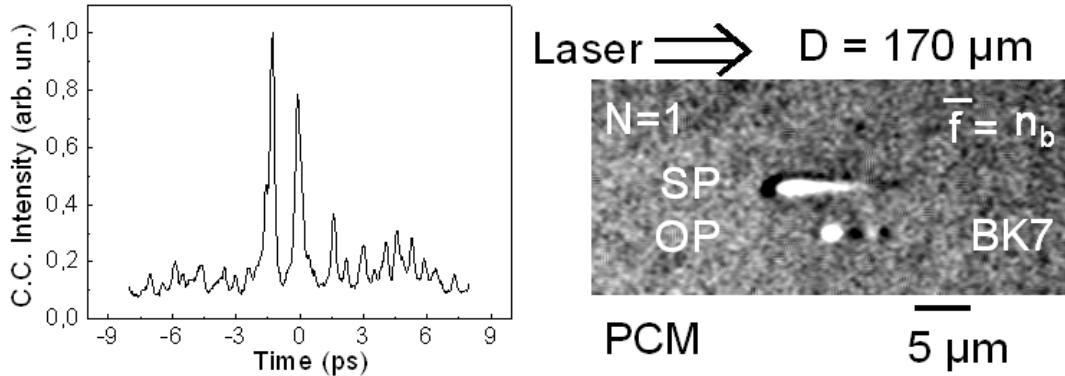
Figure 6.11: Temporal intensity distribution produced by the optimal solution (left). On the right, PCM observation of traces induced by a short pulse (SP) and an optimal pulse (OP) in a single shot regime (N=1). The laser pulse energy is limited to 350 nJ. Aberrations are minimized by focusing at D = 170 μm in the bulk.

assume that the input energy, the effective input numerical aperture (drastically depending on the diameter of the beam before the objective, see Sec. 3.2.1) and the localization of the focal plane inside the bulk are critical parameters. Finally, the second white dot systematically vanishes upon shot to shot accumulation. This is a serious limitation for performing waveguide writing. Although those pre-results are encouraging, the restrictions we noticed suggest that it would be beneficial to carry out the same experiments directly in a multishot irradiation mode.

6.5.2 Optimization on high a repetition rate system

In the prospect of achieving direct laser-processing of waveguides in BK7, there is a need for a reproducibility and a stability which has not been reached in a single-shot type of optimization (see previous section). Hence, the experimental effort was focused on optimizations in a multishot regime, close to the irradiation parameters used when writing waveguides, i.e. high number of shots. Aware of the sensitivity of BK7 to the repetition rate (see Sec. 4.2), the optimizations have been directly accomplished on a high repetition rate system.

Optimization criterion and experimental conditions

The optimizations were carried out with system IV. Each site is irradiated during 500 ms at a repetition rate of 100 kHz. Spherical aberrations were minimized by focusing the laser beam at a depth of 200 μm inside the bulk. The input energy is of about 170 nJ per pulse. Different evaluation functions were tested in order to induce a positive refractive index change in BK7.
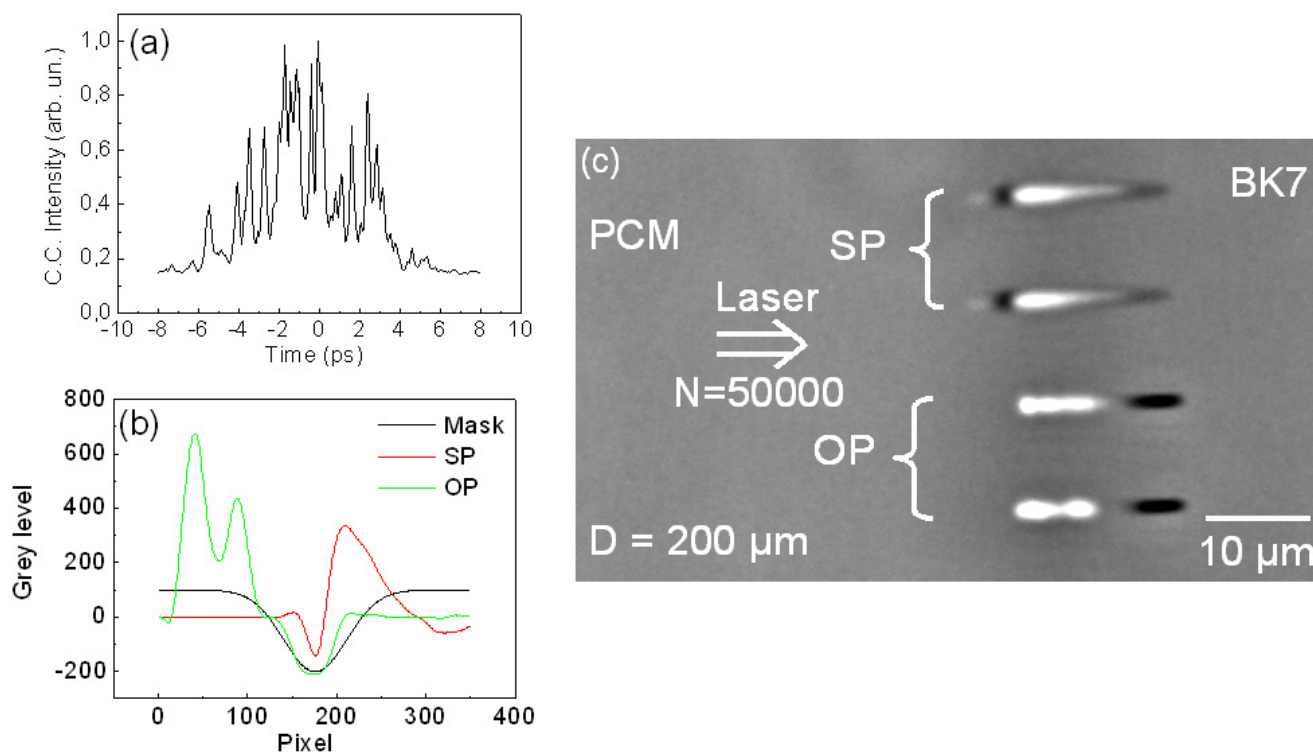
Figure 6.12: (a): Temporal intensity distribution produced by the optimal solution. (b): Comparison of the axial cross-sections induced by a short pulse (SP) and the optimal pulse (OP) with the target (left). (c): Phase contrast microscopy (PCM) observation of traces induced by the accumulation of 50000 short pulses (SP) and 50000 optimal pulses (OP) at a repetition rate of 100 kHz. The energy per pulse is limited to 170 nJ. Aberrations are minimized by focusing at D = 200 μm in the bulk.

In particular, we tried several mask targets of various widths and amplitudes to demonstrate some flexibility in the writing process.

Results

Even though up to 60 optimization runs have been carried out in excellent experimental conditions (especially regarding the laser stability), all the optimal solutions result in a very similar PCM trace. An example with a mask-based fitness function is presented in Fig. 6.12. The OTM observation does not exhibit any visible feature.

Discussion

Irrespectively on the evaluation function, white and black regions in PCM are obtained in similar proportions. The optimal temporal shape presented in Fig. 6.12 can be identified
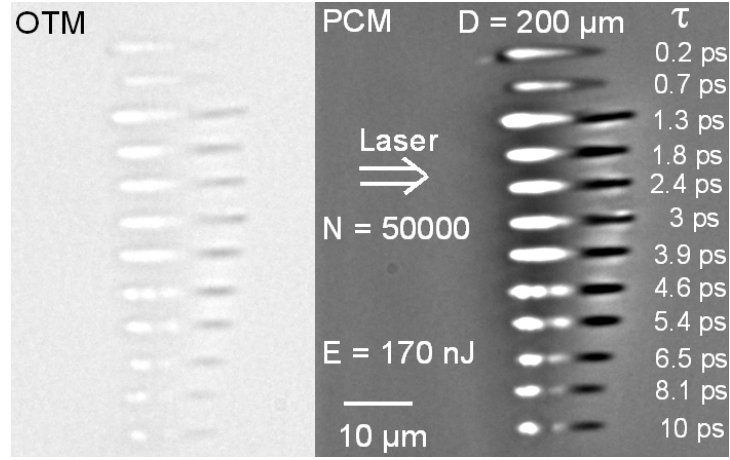
110

Figure 6.13: Aspect of traces induced by the accumulation of N=50000 chirped pulses in BK7 in OTM (left) and PCM (right). The input energy is limited to E=170 nJ. The pulse durations τ in ps are given in the right column. Aberrations are minimized by focusing at D = 200 μm in the bulk.

as a noisy picosecond envelope. This is confirmed by the resemblance of the PCM observation pictures when irradiating with the OP or with a picosecond duration pulses with a comparable input energy, as illustrated by Fig. 6.13, where the aspect of traces imprinted by laser pulses of different durations is observed in PCM. The results in OTM have also been presented, although the contrast had to be greatly enhanced to render some imprints detectable.

Based on the simulation results presented earlier (see Fig. 4.14), irradiating with laser pulse durations on the picosecond timescale results in a higher energy concentration in the vicinity of the focal plane, as the defocusing of the trailing edge of the pulse on the electron plasma generated by the leading edge of the pulse is limited (see 4.3.2). This leads to higher laser-induced glass temperatures, most likely beyond the softening point. As a result, a change in the thermomechanical response of the material is observed from the standard ultrafast irradiation regime, dominated by thermal expansion, to a regime of inelastic flow triggering material axial, unidirectional compaction. According to Fig. 6.13, this transition takes place for pulse durations between 0.7 and 1.3 ps. At the repetition rate used in this experiment (100 kHz), the material does not have enough time to relax between two consecutive pulses (see Fig. 4.11), and the material compression increases with each incoming pulse.

Comments on the search space topology

The relative uniformity of the results obtained at high repetition rates in BK7 is not very surprising. If one assumes that a 5 ps pulse corresponds to an optimum (local or global), a profusion of other optima exists in the search space, corresponding to the plethora of spectral phase patterns leading to noisy picosecond envelopes. As a consequence, the rather basic structure of one optimum results in a highly multimodal search landscape and the individuals composing the population quickly converge on one or several competing optima. Among the 60 optimization runs performed, the convergence is prematurely reached after less than 10 iterations only. Therefore, several strategies were applied to help the algorithm facing such a demanding space search topology. At first, the initial configuration parameters presented in Tab. 6.1 were modified. The main difficulty is obviously to keep a high degree of diversity within one generation. To this extent, the size of the population was doubled ($\lambda = 60$), but because of the elitist selection process, the mating pool was rapidly exclusively composed of individuals producing picosecond duration excitation profiles. Changing the mutation parameters did not bring more success and in despite of several modifications (mutation step size, adaptive mutation parameters versus single mutation step, several values of τ_{ref}), the diversity of the population invariably dropped in less than 30 iterations. In order to see whether a picosecond pulse can be optimized, an individual corresponding to a smooth picosecond pulse with a Gaussian shape (FWHM=5 ps) was introduced in the initial population. After 50 iterations, the spectral phase pattern introduced at the beginning of the optimization was almost intact and still ranked as the best individual. Finally, the compressor was detuned and a flat phase pattern was introduced in the initial population. After 30 iterations, the flat spectral phase profile was still the best individual.

Although those investigations do not prove that a picosecond pulse is a global optimum, they show that the search space is a multi-peak landscape dominated by individuals corresponding to picosecond duration Gaussian envelopes.

Perspectives

From our optimization results, there exists some flexibility via imprinting an arbitrary initial temperature map into the bulk material. The link between the temperature distribution and optimal excitation profile can be gathered by solving the nonlinear propagation model presented in Sec. 2.4.1.

The following step is to study the consequences of this controlled heating on the induced cooling dynamics in the bulk. At the present time, we initiated a collaboration with the Lavrentyev Institute of Hydrodynamics Novosibirsk (Y. Meshcheryakov), to connect the

initial temperature in the bulk with the local density of the material after cooling. The initial laser-induced temperature map is used as an input parameter in a dynamic thermal elastoplastic model.

The model takes into account heat transfer and subsequent elastoplastic response of the material to the stress induced upon diffusive cooling. The elastic part of the material response is estimated from the dynamic elasticity equations [113] and the treatment of plastic yielding is based on the Von-Mises criterion [114].

Conclusion

The intrinsic response of BK7 has been utilized in order to drive the material into higher density states upon cooling. The control over the laser-driven densification process is limited and we are not able to imprint arbitrary refractive index profiles. Nevertheless, a clear inversion of the material response is possible. The optimal excitation sequence is identified with a picosecond pulse. According to evolutionary strategy results, a pulse duration of about 5 ps FWHM gives the best results when the input energy is about 170 nJ per pulse.

The benefits of synchronizing the excitation sequence with the material response are obvious, as achieving refractive index flipping in BK7 suggests that this widely-spread glass can be potentially used as a material for laser-processing of optical structures, for the first time to our knowledge.

We further develop this aspect in the next chapter, where BK7 is used as a substrate for direct laser waveguide writing in various configurations.

6.6 Conclusion

In this chapter, the principles and the detailed implementation of an adaptive temporal pulse shaping apparatus for achieving control on laser-induced refractive index changes were presented.

At first, the experimental results we obtained have an explanatory interest. As a limitation, it is difficult to use the optimal temporal intensity distributions as a basis for understanding the mechanisms of laser-matter interaction, because nonlinear propagation does not allow a straightforward prediction of the sequential energy distribution in the focal plane. Nevertheless, we could establish, in fused silica, a correlation between presence of a high refractive index filament and void formation. This suggests that the filament may be the result of a compression triggered by a mechanical wave emitted from the void region.

Secondly, those results exhibit a potential technological interest. We demonstrated the possibility to control the spatial deposition of energy in the bulk, even in presence of strong

spherical aberrations. To this extent, temporal pulse tailoring can be promoted as an alternative to traditional methods employed to control the morphology of the laser-generated optical structures.

We also demonstrated the possibility to utilize the intrinsic response of BK7 in order to drive the material in a high density state that we could not observe when irradiating under standard ultrafast conditions. More generally, a potential is seen in writing waveguide structures in materials that do not allow it under standard short pulse irradiation.